

# Predicting the phase stability of multi-component high entropy compounds

Krishna Chaitanya Pitike,<sup>\*,†</sup> Santosh KC,<sup>‡</sup> Markus Eisenbach,<sup>¶</sup> Craig A.  
Bridges,<sup>§</sup> and Valentino R. Cooper<sup>\*,†</sup>

<sup>†</sup>*Materials Science and Technology Division, Oak Ridge National Laboratory, Oak Ridge,  
Tennessee 37831, USA*

<sup>‡</sup>*Chemical and Materials Engineering, San José State University, San José, California  
95192, USA*

<sup>¶</sup>*National Center for Computational Sciences, Oak Ridge National Laboratory, Oak Ridge,  
Tennessee 37831, USA*

<sup>§</sup>*Chemical Sciences Division, Oak Ridge National Laboratory, Oak Ridge, Tennessee 37831,  
USA*

E-mail: pitikek@ornl.gov; coopervr@ornl.gov

**NOTICE:** This manuscript has been authored by UT-Battelle, LLC, under contract DE-AC05-00OR22725 with the U.S. Department of Energy. The United States Government retains and the publisher, by accepting the article for publication, acknowledges that the United States Government retains a non-exclusive, paid-up, irrevocable, world-wide license to publish or reproduce the published form of this manuscript, or allow others to do so, for United States Government purposes. The Department of Energy will provide public access to these results of federally sponsored research in accordance with the DOE Public Access Plan (<http://energy.gov/downloads/doe-public-access-plan>).

## Abstract

A generic method to estimate the relative feasibility of formation of high entropy compounds in a single phase, directly from first principles, is developed. As a first step, the relative formation abilities of 56 multi-component,  $AO$ , oxides were evaluated. These were constructed from 5 cation combinations chosen from  $A=\{\text{Ca, Co, Cu, Fe, Mg, Mn, Ni, Zn}\}$ . Candidates for multi-component oxides are predicted from descriptors related to the enthalpy and configurational entropy obtained from the mixing enthalpies of two component oxides. The utility of this approach is evaluated by comparing the predicted combinations with the experimentally realized entropy stabilized oxide,  $(\text{MgCoCuNiZn})\text{O}$ . In the second step, Monte Carlo simulations are utilized to investigate the phase composition and local ionic segregation as a function of temperature. This approach allows for the evaluation of potential secondary phases, thereby making realistic predictions of novel multi-component compounds that can be synthesized.

## Introduction

Similar to the explosion in 2D-material systems after the first report<sup>1</sup> of graphene preparation by a simple micromechanical exfoliation of pyrolytic graphite in 2004, high entropy material synthesis is emerging as a “gold rush” for designing multi-component single phase materials. For example, high entropy (metal) alloys (HEAs) containing multi-components (generally  $\geq 5$ ) in equal atomic ratios have been demonstrated to exhibit<sup>2-6</sup> a wide range of remarkable mechanical,<sup>7-16</sup> dielectric,<sup>17</sup> and superconducting<sup>18,19</sup> properties. In some instances, the single phase multi-component materials inherit the functional traits of the parent compounds, while in other cases, they possess emergent properties due to the random/homogeneous mixing of five or more components, thus opening avenues for novel applications.

High entropy in this context may refer to the thermodynamic stabilization of a material at finite temperatures, through maximizing the entropic contributions to the free energy,

$-T\Delta S$ , rather than (or potentially in cooperation with) the mixing enthalpy,  $\Delta H_{\text{mix}}$ . In some cases, high entropy atomic substitution on a crystallographic site may not be required to stabilize a material, but may potentially impart beneficial properties beyond typically observed for the given structure type.<sup>20</sup> Building upon the success of the HEAs, researchers have attempted to synthesize ceramic analogs of the HEAs, such as high entropy oxides (HEOs). (CoCuMgNiZn)O, was the first successful multi-component oxide, and was synthesized in a pure rock salt phase.<sup>21,22</sup> In their seminal work, Rost. et al. demonstrated that an equimolar mixture of the parent oxides, CoO, CuO, MgO, NiO and ZnO, stabilizes in a pure rock salt phase at lower temperatures than any closely related off-stoichiometry composition.<sup>21</sup> Since the configurational entropy of the equimolar mixture is maximum within the ideal mixing model — correlating with the equimolar mixture exhibiting the lowest temperature at which a pure rock salt phase is stabilized — the (CoCuMgNiZn)O composition was identified as the first entropy stabilized oxide (ESO). ESO and related materials with charge compensating cationic substitutions, have demonstrated colossal dielectric constant which could be exploited for large-k dielectric materials for energy storage.<sup>17</sup> These materials are also reported to exhibit large Li-ion conductivities<sup>23</sup> and potentially large Li-storage capabilities — both of these properties are highly desirable for electrochemical energy conversion in battery applications.<sup>24-27</sup> Entropy stabilization could further benefit storage capacity retention and cycling stability in batteries.<sup>24,27</sup> Besides energy storage and electrochemical energy conversion, ESO have also been reported to exhibit long range antiferromagnetic ordering,<sup>28,29</sup> and elastic anisotropy.<sup>30</sup> Other high entropy perovskite oxides and chalcogenides show potential photocatalytic hydrogen evolution activity<sup>31</sup> and semiconducting functionalities,<sup>32</sup> respectively.

Several other multi-component compounds have since been synthesized, such as, high entropy-oxides,<sup>33-38</sup> borides,<sup>39</sup> and carbides.<sup>40-45</sup> The high entropy oxides were synthesized in several phases with, one cation sublattice structures such as, rock salt,<sup>21</sup> and fluorite,<sup>37,38</sup> as well as multi-component systems with two cation sublattices, e.g. perovskites<sup>33-35,46</sup> and

spinel.<sup>36</sup> Despite the fact that several high entropy compounds have been experimentally realized, there are > 9000 structure types (see the Inorganic Crystal Structure Database (ICSD) Ref. [47]), that could be potentially synthesized with five or more cations are present on a single crystallographic site in equal proportions. Supplementing the empirical effort, high throughput computations could accelerate the exploration of high entropy alloys and compounds. The significance of high throughput computations in materials discovery can be emphasized by recent efforts, for example, to explore ternary oxides,<sup>48</sup> water splitting catalytic activity,<sup>49</sup> battery cathode materials,<sup>50</sup> predicting phase space,<sup>51</sup> etc.

Early synthesis attempts of high entropy and entropy stabilized materials have predominantly relied on chemical intuition, based on relative atomic or ionic radii. A few previous attempts have utilized theoretical and computational methods to predict random and homogeneous mixing of multi-component high entropy alloys.<sup>52-54</sup> Some theoretical predictions<sup>55</sup> were limited to cases where a robust database, was already available, such as for metal alloys.<sup>56-59</sup> For the cases in which data were not available, computational predictions have relied on first principles based density functional theory (DFT) computations. While such computational efforts have been useful in predicting the entropy forming ability — ability/likeliness of a multi-component compound to form a single homogeneous phase — direct DFT computations suffer from not only large computational cost, but also undersampling of the configurational landscape prohibited by the size of the supercell.<sup>24</sup>

In this work, we discuss a generic method, starting from first principles, to evaluate the relative feasibility of formation of single phase multi-component compounds. Specifically, we propose enthalpy and entropy descriptors — used in quantifying the relative feasibility of formation of single phase multi-component compounds — which can be directly estimated from the mixing enthalpies of the two component compounds. A similar approach was utilized to predict the likeliness of formation of HEAs utilizing formation enthalpies of binary alloys.<sup>55</sup> Here we extend this approach to allow for the prediction of secondary phases and/or phase segregation of one or more components. This ability of this framework to dis-

cover potential secondary phases, as well as their tendency to form disordered homogeneous solid solutions allows us to make realistic predictions of novel multi-component compounds. While this work uses the example of divalent multi-component oxides, the method can be applied to other multi-component materials classes and structure types, such as: alloys, oxides (perovskites, fluorites, pyrochlores), borides, nitrides, carbides etc. Development and improvement of these methods is critical for the computational prediction and targeted experimental exploration of novel entropy stabilized materials in generic crystal structure types that could potentially be exploited in battery applications and other functionalities such as polar properties in high entropy perovskites.

## Computational Methods

### Details of first-principles calculations

All DFT calculations were carried out using the plane-wave-based Vienna *Ab-initio* Simulation Package VASP<sup>60,61</sup> version 5.4.4, within the Generalized Gradient Approximation (GGA) using the Perdew-Burke-Ernzerhof for solids (PBEsol) exchange-correlation functional.<sup>62</sup> The energy cutoff for the plane-wave basis set was 800 eV, employing Projected Augmented Wave (PAW) potentials.<sup>63,64</sup> An  $8 \times 8 \times 8$   $k$ -point mesh was utilized for sampling the Brillouin zone for a two atom unit cell and scaled linearly with the number of atoms present in the unit cell. The bulk geometry was optimized with a force convergence criterion of  $1 \text{ meV}/\text{\AA}$  and the individual components of the stress tensor were converged to  $\leq 0.1 \text{ kBar}$ .

Magnetism of Co, Cu, Fe, Mn and Ni oxides were treated with the PBEsol collinear spin density approximation in the generalized gradient approximation, with an onsite Hubbard  $U$ , (GGA+ $U$ ) scheme.<sup>65</sup> An onsite Coulomb parameter  $U = 6 \text{ eV}$  was applied for all cations to account for the increased Coulomb repulsion between the semi-filled  $3d$  states. At  $U = 6 \text{ eV}$ , we obtain a two fold advantage: first, we get the correct ground state phases for all TMOs considered, and secondly, we get insulating states for all pure and two component

oxides (TCOs). We note that, different values between  $U = 0$  and 8 eV have been used in the literature to investigate various properties of the TMOs within DFT.<sup>65-71</sup> The magnetic moments of Co, Fe, Mn and Ni oxides in the rock salt phase were initiated in the AFM-II type antiferromagnetic state (shown in Figure S1) — with spins ferromagnetically aligned within (111) planes and antiferromagnetically ordered between adjacent (111) planes.<sup>72,73</sup> These structures were also identified to have the AFM-II ground state phase within DFT and dynamical mean field theory (DMFT).<sup>65-71,74</sup>

## Nearest neighbor model

To computationally explore the configurational energy landscapes, the energies of a large number of configurations need to be studied. Sampling the configurational space directly from DFT calculations is computationally expensive and limited by the accessible supercell sizes. For example, the smallest supercell required to study (CoCuMgNiZn)O in the rock salt phase — with highly periodic cation mixing in the [1,1,1] crystallographic direction — contains 10 atoms. Whereas to obtain reasonable statistics of configurations with random cation mixing in three crystallographic directions, requires a minimum of 200 atom supercell calculations for the rock salt structure.

To reduce the computational costs associated with directly studying a five component oxide (FCO), we adopt a nearest neighbor model, (NNM) whose parameters can be relatively easily obtained from two component oxides. Essentially, the NNM defines the local energy of a cation by regarding all first nearest neighbor cations as independently interacting ions. In this picture, the interactions are limited to the first nearest neighbor cations, and solely dependent upon the composition of the first nearest neighbor cation coordination shell. It is worth noting that the interactions between the first nearest neighbor cations are mediated through the interpenetrating oxygen sublattice. The mixing enthalpies between two cations are obtained by relaxing the atomic models within DFT. Hence the mixing enthalpies of two cations implicitly include the ionic relaxation of both cation and oxygen sublattices,

arising due to the differences in the ionic radii of the cations. The enthalpies of mixing,  $\Delta H_{\text{mix}}$  between two cations in a generic phase are obtained from the DFT optimized total energies of the rock salt ordered two component oxide structures. Further information on these energetics is found below in Sec III.A. The NNM is a simple yet powerful tool to explore the potential of a composition to form ordered versus disordered structures and has been successfully utilized to study HEAs.<sup>55,75,76</sup> Here we employ the NNM as a basis for studying formation ability and local segregation in multi-component oxides.

## Results and Discussion

### Structure and enthalpies of mixing

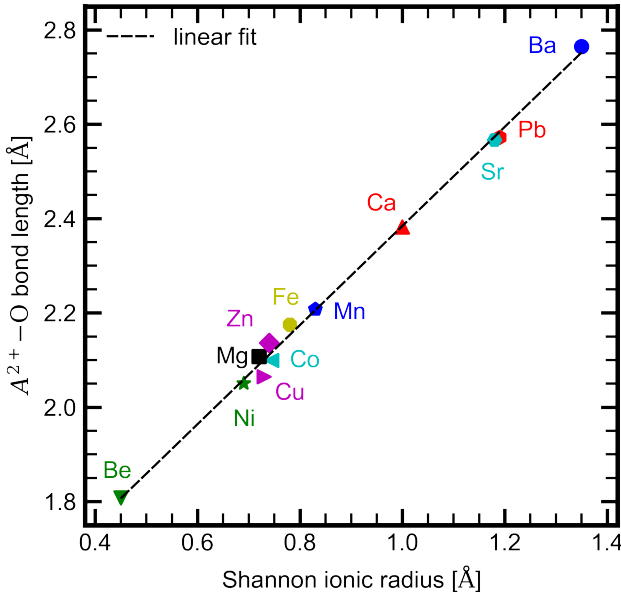


Figure 1: The Shannon ionic radii is plotted against the respective DFT computed  $A^{2+}-O$  bond length for several divalent cations in the rock salt phase. The cations constituting the original entropy stabilized oxide — Co, Cu, Mg, Ni and Zn — are clustered at the bottom of the plot, along with Fe and Mn. Whereas other cations — Ca, Sr, Ba and Pb — have large ionic radii.

Figure 1 presents the  $A-O$  bond length in the rock salt phase as a function of  $A$  cation Shannon ionic radii<sup>77</sup> for most common divalent cations — Be, Ba, Ca, Co, Cu, Fe, Mg,

Mn, Ni, Pb, Sr and Zn. As expected, the  $A$ -O bond lengths of divalent cations have strong linear correlation with their Shannon ionic radii. Interestingly we observe that the Shannon ionic radii of the cations comprising the original ESO — Co, Cu, Mg, Ni and Zn — are within 0.055 Å of each other. Chemical intuition would suggest that mixing cations with very different Shannon radii would be more likely to result in either phase segregation, or a different structure type, or the smaller cation occupying interstitial sites. Based on the  $A$ -O bond lengths (or Shannon ionic radii), in the remaining analysis, we only consider the following eight cations — Ca, Co, Cu, Fe, Mg, Mn, Ni, Zn. From these 8 cations, a total of  $8!/5!3! = 56$  five cation compositions can be generated. These 56 cations combinations along with their index are given in the supplemental information. While CaO, CoO, MgO, and NiO readily crystallize in the rock salt structure, their ground state, CuO and ZnO are stable in the tenorite and wurtzite structures, respectively. While, Fe and Mn form stable  $\text{Fe}_2\text{O}_3$  and  $\text{Mn}_2\text{O}_3$  their divalent oxides, FeO and MnO, can be experimentally realized at room temperature and ambient pressure in the rock salt structure.<sup>47,78,79</sup>

As an initial step to understanding the tendency to form a single phase solid solution we first evaluate the structure and mixing enthalpies of two component oxides,  $(AA')\text{O}$ . A total of 28 TCO compositions can be generated using the 8 divalent cations of interest ( $8!/6!2! = 28$ ). From the experimental literature, we find that the TCOs may have ground state phases in one of four structures — rock salt, tenorite, wurtzite and zinc blende. Hence, in addition to the three structure found in the parent oxides, i.e., rock salt, tenorite and wurtzite, we also consider the zinc blende structure for further analysis. Structural models of the four structures are included in the supplemental material.

The mixing enthalpy,  $\Delta H_{\text{mix}}[(AA')\text{O}, P]$ , of  $(AA')\text{O}$  TCO in a generic phase,  $P$ , is estimated from DFT calculations as shown in Eq. (1).

$$\begin{aligned} \Delta H_{\text{mix}}[(AA')\text{O}, P] = & E_{\text{DFT}}[(AA')\text{O}, P] - \frac{1}{2m} E_{\text{DFT}}[A_m\text{O}_x, \text{G}] \\ & - \frac{1}{2n} E_{\text{DFT}}[A'_n\text{O}_y, \text{G}] - \frac{1}{2} \left(1 - \frac{x}{2m} - \frac{y}{2n}\right) E_{\text{DFT}}[\text{O}_2, \text{G}] \end{aligned} \quad (1)$$

where,  $E_{\text{DFT}}[A_m\text{O}_x, G]$ ,  $E_{\text{DFT}}[A'_n\text{O}_y, G]$  are the DFT total energies of the  $A_m\text{O}_x$  and  $A'_n\text{O}_y$  oxides in their respective ground state phases.  $E_{\text{DFT}}[(AA')\text{O}, P]$  is the DFT total energy of the  $(AA')\text{O}$  TCO in phase  $P$ . In the spirit of the NNM, the value of  $E_{\text{DFT}}[(AA')\text{O}, P]$ , in its ground state phase, is used to describe the interaction energy between  $A - A'$  cations,  $\Delta H_{\text{mix}}^{A-A'} = \Delta H_{\text{mix}}[(AA')\text{O}, G]$  in the FCO.

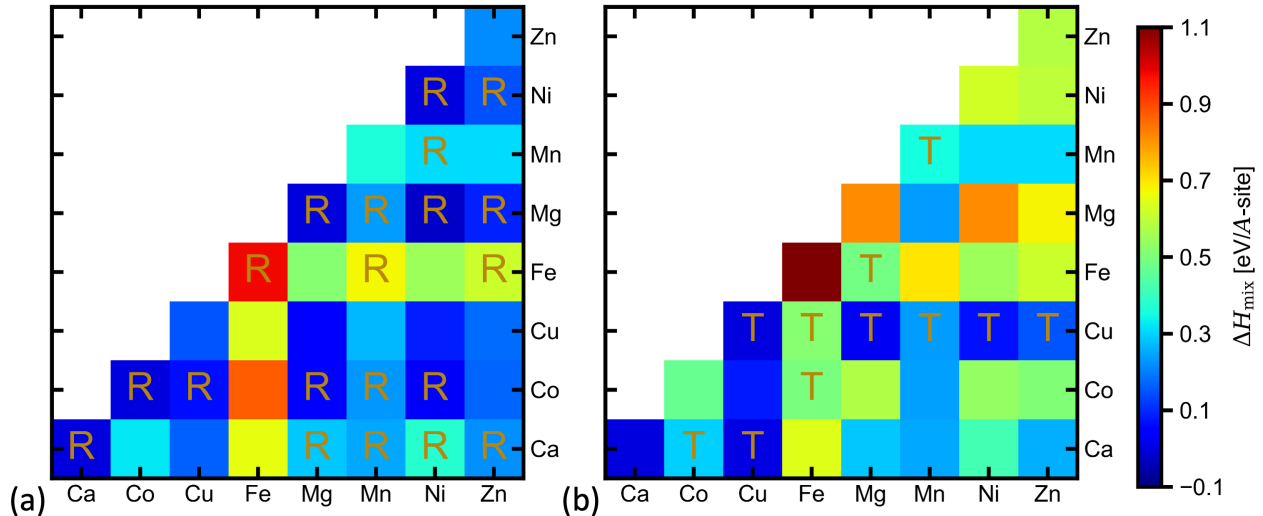


Figure 2: Heat maps for mixing enthalpy in eV/A-site of  $(AA')\text{O}$  two component oxides in phase  $P$ ,  $\Delta H_{\text{mix}}((AA')\text{O}, P)$ , calculated from first principles using Eq. (1). (a) and (b) shows the mixing enthalpy for rock salt and tenorite phases, respectively. The annotations for the rock salt and tenorite ground phases for each combination are represented with R and T, respectively. Only the lower triangular portion of the symmetric data is shown in all panels to avoid confusion. The color legend represents the mixing enthalpy in [eV/A-site] — blue and red represents low ( $\sim -0.1$ ) and high ( $\sim 1.1$ ) bond energies, respectively.

Figure 2 presents the mixing enthalpy heat maps calculated using Eq. (1). The mixing enthalpies for the rock salt, tenorite and ground phases are shown in Figure 2(a) and (b), respectively. Similar plots for the minimum energy phase, wurtzite and zinc blende phases are shown in the supplemental material. Out of these 28 unique TCO combinations and 8 parent oxides (represented by the diagonal elements), we find that there are 20, 11, 3 and 2 compounds with rock salt, tenorite, wurtzite and zinc blende minimum energy structures, respectively. Here we would like to point out that we have only considered two component oxides with equiatomic mixing in four different structures. Furthermore, a two component oxide with positive minimum energy is thermodynamically unstable and in such cases the

two component combination is more likely to form a two-phase system, either due to a lack of reaction or only a partial reaction between the components.

## Enthalpy and entropy descriptors from mixing enthalpies

The descriptors for the enthalpy and entropy, contributing to the free energy, are obtained from exploring the local mixing enthalpies within the five component oxide. In the NNM framework, the expectation value of the local mixing enthalpy of a five component oxide,  $\langle \Delta H_{\text{local}} \rangle$ , is obtained from exploring all local configurations. There are twelve first nearest neighbor cations surrounding each cation in the rock salt structure. A local atomic configuration at a lattice site,  $i$ , constitutes chemical species occupied by the lattice site,  $A^i$ , along with the twelve neighboring species,  $A^j$ ,  $j = \{1, 2, \dots, 12\}$ . This local atomic configuration is presented in the inset of Figure 3. The total number of unique local configurations are obtained by iterating through the combinations of ( $r = 5$ ) five chemically distinct cations with replacement in ( $n = 12$ ) twelve surrounding  $A$ -sites,  $N_{\text{local}} = n \times {}^{(n+r-1)}C_{(r-1)} = \frac{(n+r-1)!}{(n-1)!(r-1)!} = 9100$ . The local mixing enthalpy in the local phase  $P_i$  is estimated through,

$$\Delta H_i[\text{FCO}, P_i] = \frac{1}{n} \sum_{j=1}^n \Delta H_{\text{mix}}[(A^i A^j)\text{O}, P_i] \quad (2)$$

where,  $\Delta H_{\text{mix}}[(A^i A^j)\text{O}, P_i]$  is the average mixing enthalpy of  $A^i$  with an  $A^j$  cation species, computed from Eq. (1).

Figure 3 plots the distribution of local mixing enthalpies,  $\Delta H_i$ , in the rock salt phase for the original ESO and three representative FCOs obtained by replacing Cu by Ca, Fe and Mn. The  $\Delta H_i$  distribution for all 56 FCOs are shown in the supplemental material. The distribution of the local mixing enthalpies suggests that the number of local configurations accessible through thermal excitations are highest for the (CoCuMgNiZn)O, represented by the narrow green peak between  $E_{\text{local}} = 0.0$  and 0.2 eV. We note that the configurational entropy contribution to the Gibbs free energy should be higher for a FCO combination with

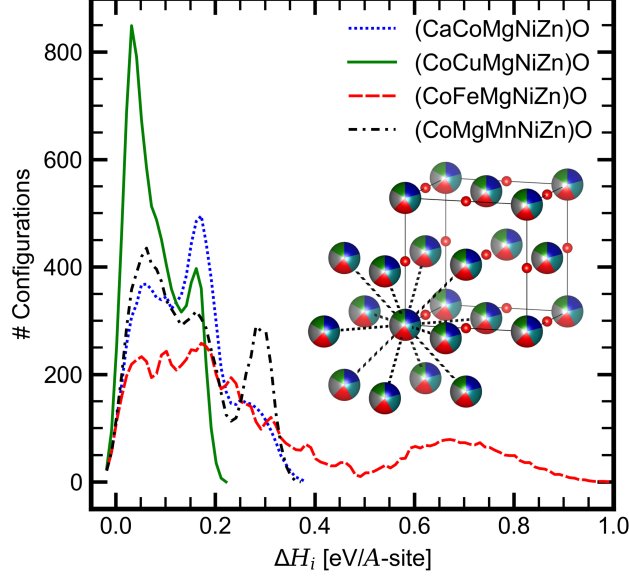


Figure 3: The energy distribution of the local mixing enthalpies of all possible configurations are plotted for four FCO combinations in rock salt phase. The solid green line shows the distribution for (CoCuMgNiZn)O. Three additional representative combinations — obtained by replacing Cu with Ca, Fe and Mg — are plotted in blue dotted, red dashed and black dot-dashed lines, respectively.

a narrow distribution of the local mixing enthalpies. The configurational entropy is inversely related to the number of configurations accessible through the thermal excitations. Further on this will be elaborated later in this section. Here, we introduce a set of descriptors that quantify the enthalpy and configurational entropy for a FCO. These are obtained from the mean,  $\mu_{\text{local}}$ , and standard deviation,  $\sigma_{\text{local}}$ , of the local mixing enthalpy distributions defined as:

$$\mu_{\text{local}} = \langle \Delta H_{\text{local}} \rangle \quad \text{and} \quad (3a)$$

$$\sigma_{\text{local}} = \sqrt{\langle \Delta H_{\text{local}}^2 \rangle - \langle \Delta H_{\text{local}} \rangle^2} ; \quad (3b)$$

$$\langle \Delta H_{\text{local}} \rangle = \frac{1}{N_{\text{local}}} \sum_{i=1}^{N_{\text{local}}} \left( \Delta H_i [\text{FCO}, P_i] \right) \quad \text{and} \quad (3c)$$

$$\langle \Delta H_{\text{local}}^2 \rangle = \frac{1}{N_{\text{local}}} \sum_{i=1}^{N_{\text{local}}} \left( \Delta H_i [\text{FCO}, P_i] \right)^2 ; \quad (3d)$$

where,  $\langle \Delta H_{\text{local}} \rangle$  and  $\langle \Delta H_{\text{local}}^2 \rangle$  are the mean values of the local mixing enthalpies and squared

local mixing enthalpies, respectively.

The significance of  $\mu_{\text{local}}$  and  $\sigma_{\text{local}}$  can be explained by considering the following two FCOs, with, (1) low- $\mu_{\text{local}}$  and low- $\sigma_{\text{local}}$ , (2) high- $\mu_{\text{local}}$  and high- $\sigma_{\text{local}}$ . For the purpose of this discussion we restrict ourselves to the case where  $\mu_{\text{local}}$  is positive, therefore indicating a preference for phase segregation, the case of  $\mu_{\text{local}}$  will be discussed later.

In the first case, the small but positive mixing enthalpy contribution to the Gibbs free energy indicates that although the compound would prefer not to form a solid solution it may be possibly overcome by entropy. Commensurately, if the distribution of configurational states is relatively narrow, i.e.  $\sigma_{\text{local}}$  is small, then the entropy contribution (which is inversely proportional to  $\sigma_{\text{local}}$ ) would be large. Here, the contributions from configurational entropy are largely due to the large number of degenerate local configurations, accessible through thermal excitations. As such, a pure single phase structure will be formed at  $T = T_t$  where the entropy contribution overcomes the small and positive enthalpy contribution. Such a case is exemplified in the the distribution of configurations for (CoCuMgNiZn)O as depicted in Fig. 3 (red dashed line).

Conversely, large  $\mu_{\text{local}}$  is indicative of a strong preference for phase segregation. However, it can be shown that in all possible FCOs from obtained by mixing 8 parent oxides, there will be at least two cations with favorable mixing enthalpies. This is suggestive of a disperse distribution of mixing enthalpies. Such a diffuse/distributed configurational landscape, would result in a very large  $\sigma_{\text{local}}$  contributing to a small configurational entropy, which will be insufficient to compensate for the already large  $\mu_{\text{local}}$ . This behavior is demonstrated in the energy distribution of (CoFeMgNiZn)O depicted in Fig. 3.

This interpretation indicates that the values of both the enthalpy and entropy descriptors,  $\mu_{\text{local}}$  and  $\sigma_{\text{local}}$ , respectively, need to be considered for predictions of formation ability of a multi-component, single phase structure. We propose that an FCO with low- $\mu_{\text{local}}$  and low- $\sigma_{\text{local}}$ , would be a prime candidate for forming a multi-component, entropy-stabilized single phase material.

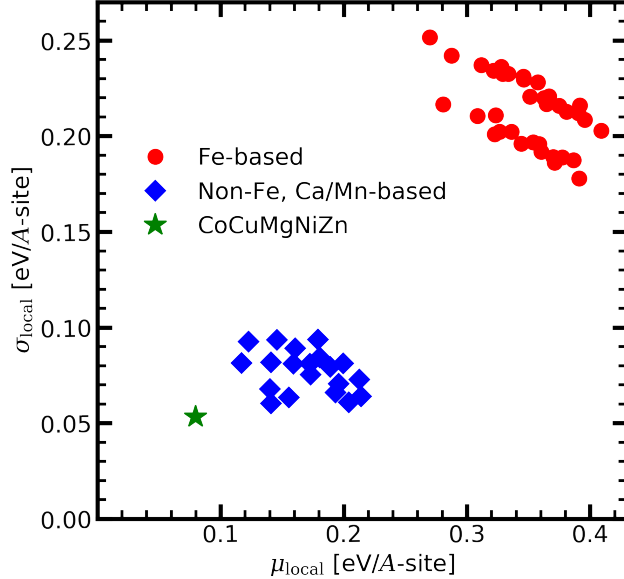


Figure 4: A comparison of the enthalpy and entropy descriptors,  $\mu_{\text{local}}$  and  $\sigma_{\text{local}}$ , respectively, for all 56 FCOs. (1) Fe-based FCO cluster is shown in red, (2) Ca- or Mn-based (without Fe) FCO cluster is shown in blue, and (3) The entropy stabilized oxide — (CoCuMgNiZn)O — shown in green, is unique FCO with least- $\mu_{\text{local}}$  and least- $\sigma_{\text{local}}$ .

Figure 4 presents a comparison of the enthalpy and entropy descriptors,  $\mu_{\text{local}}$  and  $\sigma_{\text{local}}$ , respectively, for all 56 FCOs. Surprisingly, the FCOs fall into three clusters identified by red circles, blue diamonds and a green star. First, remarkably in agreement with the experimental realization, our enthalpy and entropy descriptors, predict that the FCO represented by the green star, is distinct with  $\mu_{\text{local}}$  and  $\sigma_{\text{local}}$  close to 0; thereby having the highest potential for forming a uniform rock salt phase. Second, the 20 FCOs in the blue cluster, obtained by replacing one or two cations in the ESO with either Ca or Mn, have  $\mu_{\text{local}}$  and  $\sigma_{\text{local}}$  that range between (0.12, 0.22) eV and (0.06, 0.10) eV, respectively. On average the enthalpy contribution is higher than the ESO with a lower number of degenerate low-enthalpy configurations. The above two conditions suggests that, even large temperatures might not be sufficient for entropy to overcome the large unfavourable enthalpy. For example, the (CaCoCuMgZn)O FCO, located at the bottom of the blue cluster, has the second lowest standard deviation, only  $\Delta\sigma_{\text{local}} \sim 7 \text{ meV}/\text{\AA}$  greater than the ESO. Conversely, the mixing enthalpy of this composition is significantly  $\Delta\mu_{\text{local}} \sim 60 \text{ meV}/\text{\AA}$  greater than the ESO.

Hence, by comparing both entropy and enthalpy descriptors, we get a comprehensive picture of the formation ability and an indication of the temperature required to stabilize a single phase multi-component compound.

We find a third cluster, shown in red circles, formed from the remaining 35 Fe-based FCOs, whose values of  $\mu_{\text{local}}$  and  $\sigma_{\text{local}}$  are on the order of 0.35 eV and 0.25 eV, respectively. This indicates an extremely unfavourable mixing of Fe within the rock salt structure. The large unfavourable mixing enthalpies exhibited by Fe based FCOs — due to the strong preference of Fe to form  $\text{Fe}_2\text{O}_3$  rather than FeO — shifts the enthalpies of the local configurations up to 1 eV/ $A$ -site (shown in representative red curve in Figure 3). As discussed above, FCOs containing such configurations with large mixing enthalpies — would not be accessible to thermal excitations under the physical temperatures used for solid state reactions. The large variation in the enthalpies of Fe based FCOs results in lower configurational entropy. Similar to Fe, Mn based compounds exhibit unfavorable mixing in the rock salt phase due to its preference to form trivalent oxide, albeit the tendency is not strong as Fe. From this enthalpy and entropy descriptors, we find that the experimentally realized (CoCuMgNiZn)O is perhaps the only candidate that can form a homogeneous rock salt phase. Since the enthalpy of mixing is positive for (CoCuMgNiZn)O, the structure must be stabilized through the configurational entropy contributions, i.e. it is an entropy stabilized oxide. Following the above analysis, we possibility of forming alternate structures, i.e. tenorite, wurtzite and zinc blende. Comparisons of the enthalpy and entropy descriptors, for all 56 FCOs in the tenorite, wurtzite and zinc blende structures are shown in the supplemental material. In all cases, we find the enthalpy and entropy descriptors for the 56 FCOs in these phases to be large and positive. Thus it is highly unlikely that any binary structures considered other than rock salt, will be stabilized through entropy at experimentally accessible temperatures.

As an aside, although negative  $\mu_{\text{local}}$  was not observed for the considered FCOs, we can expect that multi-component compounds with negative mixing enthalpies exist. One scenario is that a multi-component compound may readily form a pure phase due to a large

preference of all the ions to form that common phase. Such is the case for many multi-component perovskites.<sup>33,46,80</sup> Hence in this case, the configurational entropy is not critical for the stability of the single phase. These multi-component compounds with negative mixing enthalpies cannot be considered entropy stabilized compounds.

Here, we discuss the advantages of utilizing the mixing enthalpies of TCOs to obtain entropy and enthalpy descriptors compared with alternate frameworks that were previously proposed. Sarker et. al. [35], proposed a similar approach based only on an entropy descriptor, derived from the standard deviation of the energy distribution estimated through DFT calculations on a small supercell. In their approach, the significance of the mixing enthalpy contribution — indicating the energetic favorability of mixing, which correlates with the temperature required for obtaining a pure phase — was not considered. For example, an FCO with a small  $\sigma_{\text{local}}$  could still have a large mixing enthalpy whose configurations are inaccessible through thermal excitations at physically realizable temperatures; as is the case for the (CaCoCuMgZn)O FCO discussed above. Using this approach you would have an entropy forming ability (defined as  $1/\sigma_{\text{local}}$ ) ranging from 8 to 38 (eV/atom)<sup>-1</sup>; with 38 and 33 (eV/atom)<sup>-1</sup> for the ESO and (CaCoCuMgZn)O, respectively. This would suggest formability of (CaCoCuMgZn)O without consideration of the large enthalpy of formation that would need to be overcome.

In alternate work by Troparevsky et. al. [55], a similar approach to Ref. [35], was exercised through a qualitative comparison of the “closeness” of the mixing enthalpies of binary metal alloys. Our current approach undertakes a more comprehensive analysis by computing the mean and standard deviation of the local configurational landscapes, related to the enthalpy and entropy contributions. Nevertheless, using their approach — obtained from the mean,  $\mu_{\text{mix}}$ , and standard deviation,  $\sigma_{\text{mix}}$ , of the mixing enthalpies of 15 two

component combination, as shown below:

$$\begin{aligned}\mu_{\text{mix}} &= \langle \Delta H_{\text{mix}}[(AA')\text{O}, P] \rangle \\ \sigma_{\text{mix}} &= \sqrt{\langle \Delta H_{\text{mix}}[(AA')\text{O}, P]^2 \rangle - \langle \Delta H_{\text{mix}}[(AA')\text{O}, P] \rangle^2}\end{aligned}\quad (4)$$

we find qualitative agreement for all 56 FCOs in the rock salt phases, with the ordering in Figure 4.

## Estimating the phase transition temperature through Metropolis Monte Carlo

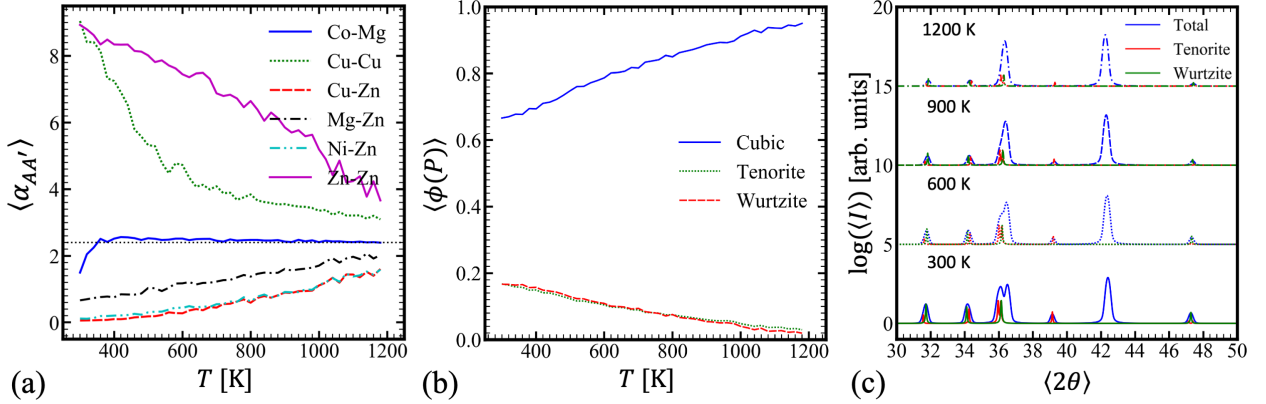


Figure 5: Shows the variation of **(a)** short range order parameter,  $\alpha_{AA'}$ , and **(b)** phase fraction,  $\phi(P)$ . **(a)** Six of the fifteen unique  $\alpha_{AA'}$  parameters are shown. All  $\alpha_{AA'}$  parameters are shown in supplemental material. **(b)** The phase fraction is shown for rock salt, tenorite and wurtzite phase. The phase fraction of rock salt phase,  $\phi(P = C)$ , increases with  $T$ , at the expense of both tenorite and wurtzite phases. **(c)** Simulated x-ray diffraction peaks, obtained from the phase fraction are shown at four different temperatures.

The enthalpy and entropy-related descriptors, discussed above, are the first step in predicting the relative likeliness of formation of an entropy stabilized phase. In this section, we assess the temperature evolution of the phase composition and cation segregation in the FCOs, specifically in,  $(\text{CoCuMgNiZn})\text{O}$  utilizing Metropolis Monte Carlo simulations on a  $5 \times 5 \times 20$  supercell that contains 2000 cations. A detailed description of the Monte Carlo method, configurational and phase composition sampling is given in the supplemental ma-

terial. Briefly, the total mixing enthalpy of the FCO lattice model microstate, in the global phase  $P$ ,  $\Delta H_{\text{total}}[\text{FCO}, P]$ , is estimated by summing over the local mixing enthalpies of all  $N = 2000$  cation lattice sites,

$$\Delta H_{\text{total}}[\text{FCO}, P] = \sum_{i=1}^N \Delta H_i[\text{FCO}, P_i] \quad (5)$$

$\Delta H_i[\text{FCO}, P_i]$  is the local mixing enthalpy at lattice site  $i$ , in the local phase  $P_i$  as described in Eq. (2). The phase composition of each microstate is achieved by assigning a local ground state phase,  $G_i$ , to each lattice site  $i$  as:

$$\Delta H_i[\text{FCO}, G_i] = \text{Min}\left(\Delta H_i[\text{FCO}, P_i]\right) \quad (6)$$

It is crucial to note that the ground state phase,  $G$ , of a microstate, is a combination of all local phases. For example, at lattice site  $i$ , a chemical species  $A^i$  is assigned a local phase  $G_i$  — which is determined based on the minimum of the mixing enthalpies of all considered phases. Defining the total energy according to Eq. (6), allows for the estimation of phase fraction,  $\phi(P)$ , of a phase  $P$ , by dividing the number of occurrences of local phase  $P_i$ , by the total number of lattice sites.

$$\phi(P) = \frac{1}{N} \sum_{i=1}^N \delta(G_i, P) \quad (7)$$

where,  $\delta(G_i, P)$  is a Dirac delta function, which returns 1 if the local ground state phase at lattice site  $i$ ,  $G_i = P$ .

While the phase fraction,  $\phi(P)$ , represents the phase composition of the microstate, it does not provide any information about local clustering of one or more cations. Any local short range ordering, representing a precipitate/secondary phase can be estimated by a short range order parameter,  $\alpha_{AA'}$ . Within the nearest neighbor model,  $\alpha_{AA'}$  can be easily estimated from a microstate by averaging the number of atoms of species  $A'$  surrounding all

atoms of species  $A$ . By the commutative relation,  $\alpha_{AA'} = \alpha_{A'A}$ , there are only fifteen unique short range order parameters in a five component high entropy compound.

Figure 5(a) depicts the variation of  $\langle \alpha_{AA'} \rangle$  as a function of  $T$ . Essentially,  $\langle \alpha_{AA'} \rangle$  represents the likelihood of finding  $A$  and  $A'$  associated with each other (if they prefer to be together,  $\langle \alpha_{AA'} \rangle$  will be larger). Here we focus on 6 of the 15 possible  $A - A'$  combinations, as shown in Figure 5(a). A more complete picture is given in Figure S6. For Mg–Co, we see that  $\langle \alpha_{\text{CoMg}} \rangle$  quickly converges to  $\sim 2.4$  at  $T = 400$  K. This is the expected value for a perfectly random FCO =  $\frac{12}{5} = 2.4$  atoms. The reader should note that, due to finite size effects, we consider ideal random mixing to be achieved when  $2 \leq \langle \alpha_{AA'} \rangle \leq 3$ . Contrarily, we observe that Zn prefers to strongly segregate with itself, evident from  $\langle \alpha_{AA'} \rangle$  decreasing to only  $\sim 4.0$  at  $T \approx 1140$  K. Other crucial observations related to each chemical species relevant to the high temperature evolution are given below.

1. Zn prefers to segregate and avoids mixing with Cu and Ni. At  $T \approx 1140$  K, Zn can accommodate  $\frac{2}{3}$  of its neighbors with other cations, typically, Mg and Co.
2. Cu avoids mixing with Zn and has a slight tendency to segregate. Cu can accommodate mixing with other cations above  $\sim 700$  K.
3. Co, Mg and Ni readily form disordered solid solutions — perhaps owing to their shared rock salt structure. First nearest neighbor interactions between the cations can incorporate Zn and Cu at higher temperatures.

Figure 5(b) illustrates the variation of  $\langle \phi(P) \rangle$  as a function of  $T$ . We find that the phase fraction of the tenorite and wurtzite phases at low temperatures  $T \sim 300$  K is  $\approx 0.2$ . The tenorite and wurtzite phases, occur in Cu and Zn rich regions of the microstate, and are indicative of their atomic fraction. Similarly, the phase fraction of the rock salt phase, at lower temperatures  $\approx 0.6$ , corresponding to the Mg, Co and Ni rich regions of the microstate, also agree with their combined atomic fraction. As the rock salt phase fraction increases to  $\approx 0.95$  at  $T \approx 1200$  K, the tenorite and wurtzite phase fractions simultaneously decrease

to  $\approx 0.03$  and  $0.02$ , respectively. These values of the phase fractions indicate that small amounts of tenorite and wurtzite phases persists even at large temperatures.

Figure 5(c) shows the simulated X-ray diffraction patterns obtained by a simple linear combination of intensities of the phases present at  $T = 300, 600, 900$  and  $1200$  K. The coefficients for the linear combination at each temperature are obtained from the phase fraction,  $\phi(P)$ . (The intensities are plotted on a log scale similar to Figure 1 in the supplemental information of Ref. [21]). Since the simulated X-ray intensities are free from noise, the tenorite+wurtzite oxygen sublattice peaks, appearing at  $2\theta = 31.6^\circ$  persevere even at  $1200$  K. Nevertheless, the relative intensities of the peaks are diminished by  $\sim 4$  and  $\sim 6$  times as the temperature is increased to  $900$  and  $1200$  K, respectively. Interestingly we find that, with the exception of the small diffraction peak near  $2\theta = 38.5^\circ$ , the wurtzite phase peaks overlap with the tenorite phase peaks.

Due to this overlap, it could be quite difficult to identify the wurtzite phase through X-ray diffraction alone. Nevertheless, our nearest neighbor model predicts that at low temperatures, the tenorite and wurtzite secondary phases coexist; decreasing with increasing temperature. This agrees well with experimentally observed phase transition from a mixed phase to a high temperature single phase.<sup>21</sup>

## Conclusions

In conclusion, we have developed a generic framework to predict high entropy materials and their potential secondary phases as a function of temperature. We achieve this by identifying, simple descriptors, to quantify the relative feasibility of formation of single phase high entropy materials. These descriptors are obtained from the statistical mean and standard deviations of local mixing enthalpies of the five component oxides. The local mixing enthalpies are computed from the mixing enthalpies of two component oxides, within the first nearest neighbor model framework, utilizing DFT calculations. In this picture, the mean is related

to the mixing enthalpy of the FCO, and the standard deviation is inversely related to the configurational entropy. Hence a multi-component system with low, positive, mean (low mixing enthalpy) and low standard deviation (high configurational entropy), should readily form a single phase high entropy compound. The proposed descriptors correctly identify the experimentally realized ESO,  $(\text{CoCuMgNiZn})\text{O}$ , as the composition most likely to form a high entropy rock salt phase. Building upon this model, we simulate the tendency of one or more components to segregate as a function of temperature through Metropolis Monte Carlo simulations. This allows us to examine phase compositions as a function of temperature. In the original ESO, we find that while Mg, Co and Ni readily form disordered solid solutions in the rock salt phase, Cu and Zn prefer to phase segregate into tenorite and wurtzite phases below  $T \sim 900$  to 1200 K, respectively.

Despite the simplicity of the nearest neighbor fixed lattice model, the model describes the configurational landscape extremely well even without including the local lattice distortions arising from random cation mixing. Ultimately, this framework is flexible and should be adaptable to other structures and chemistries, thus enabling first-principles based discovery of a wide range of entropy stabilized compounds.

## Supporting Information Available

The following files are available free of charge. Detailed description of Monte Carlo method and supporting figures are included as supplemental materials. List of all five component oxides (Table S1); mixing enthalpy values of all two component oxides within four structures (Table S2); antiferromagnetic type-II structure (Figure S1); four structural models considered in this study (Figure S2); mixing enthalpy heat maps for wurtzite and zinc blende structures (Figure S3); local enthalpy and entropy descriptors for four structures (Figure S4); mixing enthalpy and entropy descriptors for four structures (Figure S5); short range order parameters as a function of temperature for ESO (Figure S6); local mixing enthalpy

distribution for all five component combinations (Figure S7 and S8).

## Acknowledgement

This work was supported by the LDRD Program of ORNL, managed by UT-Battelle, LLC, for the U. S. DOE. This research used resources of the Oak Ridge Leadership Facility, which is a DOE Office of Science User Facility supported under contact DE-AC05-00OR22725 as well as National Energy Research Scientific Computing Center (NERSC), which is supported by the Office of Science of the U.S. Department of Energy under Contract No. DE-AC02-05CH11231. KCP and VRC acknowledge James Morris for helpful discussions. KCP acknowledges helpful discussions with German D. Samolyuk and Xianglin Liu.

## References

- (1) Novoselov, K. S. Electric Field Effect in Atomically Thin Carbon Films. *Science* **2004**, *306*, 666–669.
- (2) Ranganathan, S. Alloyed pleasures: multimetallic cocktails. *Curr. Sci.* **2003**, *85*, 1404–1406.
- (3) Yeh, J.-W.; Chen, S.-K.; Lin, S.-J.; Gan, J.-Y.; Chin, T.-S.; Shun, T.-T.; Tsau, C.-H.; Chang, S.-Y. Nanostructured High-Entropy Alloys with Multiple Principal Elements: Novel Alloy Design Concepts and Outcomes. *Advanced Engineering Materials* **2004**, *6*, 299–303.
- (4) Cantor, B.; Chang, I.; Knight, P.; Vincent, A. Microstructural development in equiatomic multicomponent alloys. *Materials Science and Engineering: A* **2004**, *377*, 213–218.

- (5) Senkov, O.; Miller, J.; Miracle, D.; Woodward, C. Accelerated exploration of multi-principal element alloys with solid solution phases. *Nature Communications* **2015**, *6*.
- (6) Widom, M. Modeling the structure and thermodynamics of high-entropy alloys. *Journal of Materials Research* **2018**, *33*, 2881–2898.
- (7) Gao, M. C., Yeh, J.-W., Liaw, P. K., Zhang, Y., Eds. *High-Entropy Alloys*; Springer International Publishing, 2016.
- (8) Lim, X. Mixed-up metals make for stronger, tougher, stretchier alloys. *Nature* **2016**, *533*, 306–307.
- (9) Gludovatz, B.; Hohenwarter, A.; Catoor, D.; Chang, E. H.; George, E. P.; Ritchie, R. O. A fracture-resistant high-entropy alloy for cryogenic applications. *Science* **2014**, *345*, 1153–1158.
- (10) Gali, A.; George, E. Tensile properties of high- and medium-entropy alloys. *Intermetallics* **2013**, *39*, 74–78.
- (11) Senkov, O.; Wilks, G.; Scott, J.; Miracle, D. Mechanical properties of Nb<sub>25</sub>Mo<sub>25</sub>Ta<sub>25</sub>W<sub>25</sub> and V<sub>20</sub>Nb<sub>20</sub>Mo<sub>20</sub>Ta<sub>20</sub>W<sub>20</sub> refractory high entropy alloys. *Intermetallics* **2011**, *19*, 698–706.
- (12) Li, Z.; Pradeep, K. G.; Deng, Y.; Raabe, D.; Tasan, C. C. Metastable high-entropy dual-phase alloys overcome the strength–ductility trade-off. *Nature* **2016**, *534*, 227–230.
- (13) Tsao, T.-K.; Yeh, A.-C.; Kuo, C.-M.; Kakehi, K.; Murakami, H.; Yeh, J.-W.; Jian, S.-R. The High Temperature Tensile and Creep Behaviors of High Entropy Superalloy. *Scientific Reports* **2017**, *7*.
- (14) Li, Z.; Tasan, C. C.; Springer, H.; Gault, B.; Raabe, D. Interstitial atoms enable

- joint twinning and transformation induced plasticity in strong and ductile high-entropy alloys. *Scientific Reports* **2017**, *7*.
- (15) Senkov, O.; Wilks, G.; Miracle, D.; Chuang, C.; Liaw, P. Refractory high-entropy alloys. *Intermetallics* **2010**, *18*, 1758–1765.
- (16) Senkov, O.; Senkova, S.; Woodward, C.; Miracle, D. Low-density, refractory multi-principal element alloys of the Cr–Nb–Ti–V–Zr system: Microstructure and phase analysis. *Acta Materialia* **2013**, *61*, 1545–1557.
- (17) Bérardan, D.; Franger, S.; Dragoë, D.; Meena, A. K.; Dragoë, N. Colossal dielectric constant in high entropy oxides. *physica status solidi (RRL) - Rapid Research Letters* **2016**, *10*, 328–333.
- (18) von Rohr, F.; Winiarski, M. J.; Tao, J.; Klimczuk, T.; Cava, R. J. Effect of electron count and chemical complexity in the Ta–Nb–Hf–Zr–Ti high-entropy alloy superconductor. *Proceedings of the National Academy of Sciences* **2016**, *113*, E7144–E7150.
- (19) Stolze, K.; Tao, J.; von Rohr, F. O.; Kong, T.; Cava, R. J. Sc–Zr–Nb–Rh–Pd and Sc–Zr–Nb–Ta–Rh–Pd High-Entropy Alloy Superconductors on a CsCl-Type Lattice. *Chemistry of Materials* **2018**, *30*, 906–914.
- (20) Oses, C.; Toher, C.; Curtarolo, S. High-entropy ceramics. *Nature Reviews Materials* **2020**, *5*, 295–309.
- (21) Rost, C. M.; Sachet, E.; Borman, T.; Moballeggh, A.; Dickey, E. C.; Hou, D.; Jones, J. L.; Curtarolo, S.; Maria, J.-P. Entropy-stabilized oxides. *Nature Communications* **2015**, *6*.
- (22) Rak, Z.; Rost, C. M.; Lim, M.; Sarker, P.; Toher, C.; Curtarolo, S.; Maria, J.-P.; Brenner, D. W. Charge compensation and electrostatic transferability in three entropy-

- stabilized oxides: Results from density functional theory calculations. *Journal of Applied Physics* **2016**, *120*, 095105.
- (23) Bérardan, D.; Franger, S.; Meena, A. K.; Dragoë, N. Room temperature lithium superionic conductivity in high entropy oxides. *Journal of Materials Chemistry A* **2016**, *4*, 9536–9541.
- (24) Sarkar, A.; Velasco, L.; Wang, D.; Wang, Q.; Talasila, G.; de Biasi, L.; Kbel, C.; Brezesinski, T.; Bhattacharya, S. S.; Hahn, H.; Breitung, B. High entropy oxides for reversible energy storage. *Nature Communications* **2018**, *9*.
- (25) Sarkar, A.; Wang, Q.; Schiele, A.; Chellali, M. R.; Bhattacharya, S. S.; Wang, D.; Brezesinski, T.; Hahn, H.; Velasco, L.; Breitung, B. High-Entropy Oxides: Fundamental Aspects and Electrochemical Properties. *Advanced Materials* **2019**, *31*, 1806236.
- (26) Wang, Q.; Sarkar, A.; Li, Z.; Lu, Y.; Velasco, L.; Bhattacharya, S. S.; Brezesinski, T.; Hahn, H.; Breitung, B. High entropy oxides as anode material for Li-ion battery applications: A practical approach. *Electrochemistry Communications* **2019**, *100*, 121–125.
- (27) Lkç, E.; Toparli, Ç.; Anik, M. Electrochemical Performance of  $(\text{MgCoNiZn})_{1-x}\text{Li}_x\text{O}$  High-Entropy Oxides in Lithium-Ion Batteries. *ACS Applied Materials & Interfaces* **2020**, *12*, 23860–23866.
- (28) Zhang, J.; Yan, J.; Calder, S.; Zheng, Q.; McGuire, M. A.; Abernathy, D. L.; Ren, Y.; Lapidus, S. H.; Page, K.; Zheng, H.; Freeland, J. W.; Budai, J. D.; Hermann, R. P. Long-Range Antiferromagnetic Order in a Rocksalt High Entropy Oxide. *Chemistry of Materials* **2019**, *31*, 3705–3711.
- (29) Frandsen, B. A.; Petersen, K. A.; Ducharme, N. A.; Shaw, A. G.; Gibson, E. J.; Winn, B.; Yan, J.; Zhang, J.; Manley, M. E.; Hermann, R. P. Spin dynamics and a nearly continuous magnetic phase transition in an entropy-stabilized oxide antiferromagnet. *arXiv preprint arXiv:2004.04218 (accepted in Phys. Rev. Mater.)*

- (30) Pitike, K. C.; Marquez-Rossy, A.; Flores-Betancourt, A.; Chen, D. X.; KC, S.; Cooper, V. R.; Lara-Curzio, E. On the Elastic Anisotropy of the Entropy-Stabilized Oxide (Mg, Co, Ni, Cu, Zn)O. *arXiv preprint arXiv:2004.06613 (accepted in J. Appl. Phys.)*
- (31) Edalati, P.; Wang, Q.; Razavi-Khosroshahi, H.; Fuji, M.; Ishihara, T.; Edalati, K. Photocatalytic hydrogen evolution on a high-entropy oxide. *Journal of Materials Chemistry A* **2020**, *8*, 3814–3821.
- (32) Deng, Z.; Olvera, A.; Casamento, J.; Lopez, J. S.; Williams, L.; Lu, R.; Shi, G.; Poudeu, P. F. P.; Kioupakis, E. Semiconducting High-Entropy Chalcogenide Alloys with Ambi-ionic Entropy Stabilization and Ambipolar Doping. *Chemistry of Materials* **2020**,
- (33) Sharma, Y.; Musico, B. L.; Gao, X.; Hua, C.; May, A. F.; Herklotz, A.; Rastogi, A.; Mandrus, D.; Yan, J.; Lee, H. N.; Chisholm, M. F.; Keppens, V.; Ward, T. Z. Single-crystal high entropy perovskite oxide epitaxial films. *Physical Review Materials* **2018**, *2*.
- (34) Jiang, S.; Hu, T.; Gild, J.; Zhou, N.; Nie, J.; Qin, M.; Harrington, T.; Vecchio, K.; Luo, J. A new class of high-entropy perovskite oxides. *Scripta Materialia* **2018**, *142*, 116–120.
- (35) Sarkar, A.; Djenadic, R.; Wang, D.; Hein, C.; Kautenburger, R.; Clemens, O.; Hahn, H. Rare earth and transition metal based entropy stabilised perovskite type oxides. *Journal of the European Ceramic Society* **2018**, *38*, 2318–2327.
- (36) Dabrowa, J.; Stygar, M.; Mikula, A.; Knapik, A.; Mroczka, K.; Tejchman, W.; Danielewski, M.; Martin, M. Synthesis and microstructure of the (Co,Cr,Fe,Mn,Ni)<sub>3</sub>O<sub>4</sub> high entropy oxide characterized by spinel structure. *Materials Letters* **2018**, *216*, 32–36.

- (37) Gild, J.; Samiee, M.; Braun, J. L.; Harrington, T.; Vega, H.; Hopkins, P. E.; Vecchio, K.; Luo, J. High-entropy fluorite oxides. *Journal of the European Ceramic Society* **2018**, *38*, 3578–3584.
- (38) Chen, K.; Pei, X.; Tang, L.; Cheng, H.; Li, Z.; Li, C.; Zhang, X.; An, L. A five-component entropy-stabilized fluorite oxide. *Journal of the European Ceramic Society* **2018**, *38*, 4161–4164.
- (39) Gild, J.; Zhang, Y.; Harrington, T.; Jiang, S.; Hu, T.; Quinn, M. C.; Mellor, W. M.; Zhou, N.; Vecchio, K.; Luo, J. High-Entropy Metal Diborides: A New Class of High-Entropy Materials and a New Type of Ultrahigh Temperature Ceramics. *Scientific Reports* **2016**, *6*.
- (40) Castle, E.; Csanádi, T.; Grasso, S.; Dusza, J.; Reece, M. Processing and Properties of High-Entropy Ultra-High Temperature Carbides. *Scientific Reports* **2018**, *8*.
- (41) Dusza, J.; Švec, P.; Girman, V.; Sedlák, R.; Castle, E. G.; Csanádi, T.; Kovalčíková, A.; Reece, M. J. Microstructure of (Hf-Ta-Zr-Nb)C high-entropy carbide at micro and nano/atomic level. *Journal of the European Ceramic Society* **2018**, *38*, 4303–4307.
- (42) Yan, X.; Constantin, L.; Lu, Y.; Silvain, J.-F.; Nastasi, M.; Cui, B. (Hf 0.2 Zr 0.2 Ta 0.2 Nb 0.2 Ti 0.2 )C high-entropy ceramics with low thermal conductivity. *Journal of the American Ceramic Society* **2018**, *101*, 4486–4491.
- (43) Zhou, J.; Zhang, J.; Zhang, F.; Niu, B.; Lei, L.; Wang, W. High-entropy carbide: A novel class of multicomponent ceramics. *Ceramics International* **2018**, *44*, 22014–22018.
- (44) Sarker, P.; Harrington, T.; Toher, C.; Oses, C.; Samiee, M.; Maria, J.-P.; Brenner, D. W.; Vecchio, K. S.; Curtarolo, S. High-entropy high-hardness metal carbides discovered by entropy descriptors. *Nature Communications* **2018**, *9*.

- (45) Zhang, R.-Z.; Reece, M. J. Review of high entropy ceramics: design, synthesis, structure and properties. *Journal of Materials Chemistry A* **2019**, *7*, 22148–22162.
- (46) Brahlek, M.; Mazza, A. R.; Pitike, K. C.; Skoropata, E.; Lapano, J.; Eres, G.; Cooper, V. R.; Ward, T. Z. Unexpected crystalline homogeneity from the disordered bond network in  $\text{La}(\text{Cr}_{0.2}\text{Mn}_{0.2}\text{Fe}_{0.2}\text{Co}_{0.2}\text{Ni}_{0.2})\text{O}_3$  films. *Phys. Rev. Materials* **2020**, *4*, 054407.
- (47) Bergerhoff, G.; Brown, I.; Allen, F., et al. Crystallographic databases. *International Union of Crystallography, Chester* **1987**, *360*, 77–95.
- (48) Hautier, G.; Fischer, C. C.; Jain, A.; Mueller, T.; Ceder, G. Finding Nature’s Missing Ternary Oxide Compounds Using Machine Learning and Density Functional Theory. *Chemistry of Materials* **2010**, *22*, 3762–3767.
- (49) Emery, A. A.; Saal, J. E.; Kirklin, S.; Hegde, V. I.; Wolverton, C. High-Throughput Computational Screening of Perovskites for Thermochemical Water Splitting Applications. *Chemistry of Materials* **2016**, *28*, 5621–5634.
- (50) Hautier, G.; Jain, A.; Ong, S. P.; Kang, B.; Moore, C.; Doe, R.; Ceder, G. Phosphates as Lithium-Ion Battery Cathodes: An Evaluation Based on High-Throughput ab Initio Calculations. *Chemistry of Materials* **2011**, *23*, 3495–3508.
- (51) Ong, S. P.; Wang, L.; Kang, B.; Ceder, G. Li-Fe-P-O<sub>2</sub> Phase Diagram from First Principles Calculations. *Chemistry of Materials* **2008**, *20*, 1798–1807.
- (52) Huang, W.; Martin, P.; Zhuang, H. L. Machine-learning phase prediction of high-entropy alloys. *Acta Materialia* **2019**, *169*, 225–236.
- (53) Yang, X.; Zhang, Y. Prediction of high-entropy stabilized solid-solution in multi-component alloys. *Materials Chemistry and Physics* **2012**, *132*, 233–238.

- (54) Chattopadhyay, C.; Prasad, A.; Murty, B. Phase prediction in high entropy alloys – A kinetic approach. *Acta Materialia* **2018**, *153*, 214–225.
- (55) Troparevsky, M. C.; Morris, J. R.; Kent, P. R.; Lupini, A. R.; Stocks, G. M. Criteria for Predicting the Formation of Single-Phase High-Entropy Alloys. *Physical Review X* **2015**, *5*.
- (56) Curtarolo, S.; Morgan, D.; Persson, K.; Rodgers, J.; Ceder, G. Predicting Crystal Structures with Data Mining of Quantum Calculations. *Physical Review Letters* **2003**, *91*.
- (57) Curtarolo, S.; Setyawan, W.; Hart, G. L.; Jahnatek, M.; Chepulskii, R. V.; Taylor, R. H.; Wang, S.; Xue, J.; Yang, K.; Levy, O.; Mehl, M. J.; Stokes, H. T.; Demchenko, D. O.; Morgan, D. AFLOW: An automatic framework for high-throughput materials discovery. *Computational Materials Science* **2012**, *58*, 218–226.
- (58) Curtarolo, S.; Hart, G. L. W.; Nardelli, M. B.; Mingo, N.; Sanvito, S.; Levy, O. The high-throughput highway to computational materials design. *Nature Materials* **2013**, *12*, 191–201.
- (59) Hart, G. L. W.; Curtarolo, S.; Massalski, T. B.; Levy, O. Comprehensive Search for New Phases and Compounds in Binary Alloy Systems Based on Platinum-Group Metals, Using a Computational First-Principles Approach. *Physical Review X* **2013**, *3*.
- (60) Kresse, G.; Furthmüller, J. Efficiency of ab-initio total energy calculations for metals and semiconductors using a plane-wave basis set. *Computational Materials Science* **1996**, *6*, 15–50.
- (61) Kresse, G.; Furthmüller, J. Efficient iterative schemes for ab initio total-energy calculations using a plane-wave basis set. *Physical Review B* **1996**, *54*, 11169–11186.

- (62) Perdew, J. P.; Ruzsinszky, A.; Csonka, G. I.; Vydrov, O. A.; Scuseria, G. E.; Constantin, L. A.; Zhou, X.; Burke, K. Restoring the Density-Gradient Expansion for Exchange in Solids and Surfaces. *Physical Review Letters* **2008**, *100*.
- (63) Blchl, P. E. Projector augmented-wave method. *Physical Review B* **1994**, *50*, 17953–17979.
- (64) Kresse, G.; Joubert, D. From ultrasoft pseudopotentials to the projector augmented-wave method. *Physical Review B* **1999**, *59*, 1758–1775.
- (65) Dudarev, S. L.; Botton, G. A.; Savrasov, S. Y.; Humphreys, C. J.; Sutton, A. P. Electron-energy-loss spectra and the structural stability of nickel oxide: An LSDA+U study. *Physical Review B* **1998**, *57*, 1505–1509.
- (66) Franchini, C.; Bayer, V.; Podloucky, R.; Paier, J.; Kresse, G. Density functional theory study of MnO by a hybrid functional approach. *Physical Review B* **2005**, *72*.
- (67) Fang, Z.; Solovyev, I. V.; Sawada, H.; Terakura, K. First-principles study on electronic structures and phase stability of MnO and FeO under high pressure. *Physical Review B* **1999**, *59*, 762–774.
- (68) Cococcioni, M.; de Gironcoli, S. Linear response approach to the calculation of the effective interaction parameters in theLDA+U method. *Phys. Rev. B* **2005**, *71*.
- (69) Boussendel, A.; Baadji, N.; Haroun, A.; Dreysse, H.; Alouani, M. Effect of substrate strain on calculated magnetic properties and magnetic anisotropy energy of CoO. *Physical Review B* **2010**, *81*.
- (70) Schrn, A.; Rdl, C.; Bechstedt, F. Crystalline and magnetic anisotropy of the 3d-transition metal monoxides MnO, FeO, CoO, and NiO. *Physical Review B* **2012**, *86*.

- (71) Deng, H.-X.; Li, J.; Li, S.-S.; Xia, J.-B.; Walsh, A.; Wei, S.-H. Origin of antiferromagnetism in CoO: A density functional theory study. *Applied Physics Letters* **2010**, *96*, 162508.
- (72) Shull, C. G.; Strauser, W. A.; Wollan, E. O. Neutron Diffraction by Paramagnetic and Antiferromagnetic Substances. *Physical Review* **1951**, *83*, 333–345.
- (73) Roth, W. L. Magnetic Structures of MnO, FeO, CoO, and NiO. *Physical Review* **1958**, *110*, 1333–1341.
- (74) Zhang, L.; Staar, P.; Kozhevnikov, A.; Wang, Y.-P.; Trinastic, J.; Schulthess, T.; Cheng, H.-P. DFT+DMFT calculations of the complex band and tunneling behavior for the transition metal monoxides MnO, FeO, CoO, and NiO. *Physical Review B* **2019**, *100*.
- (75) Hillert, M. On the nearest neighbour interaction model with a concentration dependent interaction energy. *Journal de Physique et le Radium* **1962**, *23*, 835–840.
- (76) Santodonato, L. J.; Liaw, P. K.; Unocic, R. R.; Bei, H.; Morris, J. R. Predictive multiphase evolution in Al-containing high-entropy alloys. *Nature Communications* **2018**, *9*.
- (77) Shannon, R. D. Revised effective ionic radii and systematic studies of interatomic distances in halides and chalcogenides. *Acta Crystallographica Section A* **1976**, *32*, 751–767.
- (78) Katsura, T.; Iwasaki, B.; Kimura, S.; Ito, Akimoto, S. High-Pressure Synthesis of the Stoichiometric Compound FeO. *The Journal of Chemical Physics* **1967**, *47*, 4559–4560.
- (79) Sasaki, S.; Fijino, K.; Takéuchi, Y. X-Ray Determination of Electron-Density Distributions in Oxides, MgO, MnO, CoO, and NiO, and Atomic Scattering Factors of their

Constituent Atoms. *Proceedings of the Japan Academy. Ser. B: Physical and Biological Sciences* **1979**, *55*, 43–48.

- (80) Takayama-Muromachi, E.; Navrotsky, A. Energetics of compounds ( $A^{2+}B^{4+}O_3$ ) with the perovskite structure. *Journal of Solid State Chemistry* **1988**, *72*, 244–256.

# Supporting information: Predicting the phase stability of multi-component high entropy compounds

## Metropolis Monte Carlo simulation details

Utilizing the nearest neighbor model discussed in the main text, we employed Metropolis Monte Carlo simulations to study the mixing behaviour between different chemical species within the FCO at relevant temperatures ranging from  $T = 300$  to  $1200$  K. Atomic configurations — generated through randomly swapping unlike atoms between different lattice sites in a  $5 \times 5 \times 20$  periodic supercell (total 2000 cations) — are sampled according to the Metropolis criterion. The simulation is started from a random atomic configuration. A trial configuration is accepted according to the Boltzmann probability,  $p_B$ ,

$$p_B = \text{Min} \left\{ \exp \left( \frac{-\Delta H}{k_B T} \right), 1 \right\} \quad (8)$$

where,  $\Delta H = (\Delta H_{\text{total}}^n - \Delta H_{\text{total}}^{n-1})$  is the change in total mixing enthalpy between  $n^{\text{th}}$  and  $n - 1^{\text{th}}$  steps, caused by swapping unlike chemical species.  $k_B$  is Boltzmann constant and  $T$  is absolute temperature. The trial configuration is always accepted if  $\Delta H \leq 0$ . However, if  $\Delta H > 0$  the trial configuration is accepted by chance, according to the Boltzmann probability,  $p_B$ .

In addition to the Metropolis sampling of atomic configurations, we also assign the phase composition, by assigning a “global” phase  $P = \{G, R, T, W, Z\}$ , to the atomic configuration. While  $P = G$  represents mixture of multiple phases in the lattice model, whose phase fractions are estimated using Eq. (7) in the main text,  $P = \{R, T, W, Z\}$  represents pure rock salt, tenorite, wurtzite and Zinc blende phases, respectively. Two schemes were tested

to update the phase composition of the configuration, both resulting in approximately equal phase compositions and short range order parameter trends as a function of  $T$ . In the first scheme, the phase composition is updated after  $N_p$  atomic updates, according to the metropolis criterion. For example, the phase is updated from  $P = \text{G}$  to  $P = \text{R}$  according to the Boltzmann probability,  $p_B$ , where,

$$\Delta H = \Delta H_{\text{total}}^n[\text{FCO}, \text{R}] - \Delta H_{\text{total}}^n[\text{FCO}, \text{G}], \quad (9)$$

is the energy difference between the configuration in pure rock salt phase and the ground phase with mixed phase composition. The results did not change significantly between  $N_p = 5$  and 2.

In the second scheme, the phase is updated from the ground phase to the pure phase at each step, according the Boltzmann probability, where,

$$\Delta H = \Delta H_{\text{total}}^n[\text{FCO}, \text{R}] - \Delta H_{\text{total}}^{n-1}[\text{FCO}, \text{G}], \quad (10)$$

measures the energy difference between the trail configuration in the rock salt phase and the previous confuration in ground phase. The Monte Carlo simulation is ran isothermally at several temperature values within a relevant temperature range. The expectation values of phase fraction  $\langle \phi(P) \rangle$  and short range order parameter  $\langle \alpha_{AA'} \rangle$  are estimated for each simulation at constant temperature.

Table S1: List of five component combinations chosen from set of cations,  $A=\{\text{Ca, Co, Cu, Fe, Mg, Mn, Ni, Zn}\}$ .

Index	Combination	Index	Combination
1	CaCoCuFeMg	29	CaCuMgNiZn
2	CaCoCuFeMn	30	CaCuMnNiZn
3	CaCoCuFeNi	31	CaFeMgMnNi
4	CaCoCuFeZn	32	CaFeMgMnZn
5	CaCoCuMgMn	33	CaFeMgNiZn
6	CaCoCuMgNi	34	CaFeMnNiZn
7	CaCoCuMgZn	35	CaMgMnNiZn
8	CaCoCuMnNi	36	CoCuFeMgMn
9	CaCoCuMnZn	37	CoCuFeMgNi
10	CaCoCuNiZn	38	CoCuFeMgZn
11	CaCoFeMgMn	39	CoCuFeMnNi
12	CaCoFeMgNi	40	CoCuFeMnZn
13	CaCoFeMgZn	41	CoCuFeNiZn
14	CaCoFeMnNi	42	CoCuMgMnNi
15	CaCoFeMnZn	43	CoCuMgMnZn
16	CaCoFeNiZn	44	CoCuMgNiZn
17	CaCoMgMnNi	45	CoCuMnNiZn
18	CaCoMgMnZn	46	CoFeMgMnNi
19	CaCoMgNiZn	47	CoFeMgMnZn
20	CaCoMnNiZn	48	CoFeMgNiZn
21	CaCuFeMgMn	49	CoFeMnNiZn
22	CaCuFeMgNi	50	CoMgMnNiZn
23	CaCuFeMgZn	51	CuFeMgMnNi
24	CaCuFeMnNi	52	CuFeMgMnZn
25	CaCuFeMnZn	53	CuFeMgNiZn
26	CaCuFeNiZn	54	CuFeMnNiZn
27	CaCuMgMnNi	55	CuMgMnNiZn
28	CaCuMgMnZn	56	FeMgMnNiZn

Table S2: Mixing enthalpy values of two component oxides computed from DFT in eV/A-site.

Index	TCO	Rock salt	Tenorite	Wurtzite	Zinc blende	Ground phase
1	Ca-Ca	0.000	0.000	0.015	0.038	Rock salt
2	Ca-Co	0.027	0.025	0.033	0.039	Tenorite
3	Ca-Cu	0.014	0.000	0.029	0.041	Tenorite
4	Ca-Fe	0.055	0.053	0.066	0.044	Zinc blende
5	Ca-Mg	0.024	0.024	0.039	0.045	Rock salt
6	Ca-Mn	0.021	0.021	0.033	0.045	Rock salt
7	Ca-Ni	0.031	0.035	0.035	0.034	Rock salt
8	Ca-Zn	0.018	0.021	0.027	0.031	Rock salt
9	Co-Co	0.000	0.039	0.009	0.011	Rock salt
10	Co-Cu	0.005	0.007	0.054	0.052	Rock salt
11	Co-Fe	0.073	0.042	0.055	0.058	Tenorite
12	Co-Mg	0.003	0.048	0.014	0.019	Rock salt
13	Co-Mn	0.019	0.020	0.029	0.030	Rock salt
14	Co-Ni	0.002	0.044	0.031	0.033	Rock salt
15	Co-Zn	0.014	0.042	0.005	0.006	Wurtzite
16	Cu-Cu	0.013	0.000	0.057	0.052	Tenorite
17	Cu-Fe	0.053	0.043	0.072	0.068	Tenorite
18	Cu-Mg	0.004	0.002	0.039	0.040	Tenorite
19	Cu-Mn	0.022	0.020	0.056	0.057	Tenorite
20	Cu-Ni	0.007	0.006	0.055	0.056	Tenorite
21	Cu-Zn	0.015	0.012	0.028	0.029	Tenorite
22	Fe-Fe	0.082	0.103	0.092	0.082	Rock salt
23	Fe-Mg	0.043	0.041	0.072	0.074	Tenorite

Continued on next page

**Table S2 – continued from previous page**

Index	TCO	Rock salt	Tenorite	Wurtzite	Zinc blende	Ground phase
24	Fe-Mn	0.056	0.058	0.066	0.084	Rock salt
25	Fe-Ni	0.046	0.046	0.067	0.044	Zinc blende
26	Fe-Zn	0.051	0.051	0.062	0.063	Rock salt
27	Mg-Mg	-0.000	0.068	0.020	0.026	Rock salt
28	Mg-Mn	0.020	0.020	0.033	0.036	Rock salt
29	Mg-Ni	-0.002	0.068	0.003	0.069	Rock salt
30	Mg-Zn	0.007	0.057	0.009	0.012	Rock salt
31	Mn-Mn	0.030	0.029	0.043	0.045	Tenorite
32	Mn-Ni	0.026	0.026	0.030	0.028	Rock salt
33	Mn-Zn	0.026	0.026	0.024	0.025	Wurtzite
34	Ni-Ni	0.000	0.052	0.010	0.056	Rock salt
35	Ni-Zn	0.012	0.050	0.026	0.028	Rock salt
36	Zn-Zn	0.018	0.048	0.000	0.001	Wurtzite

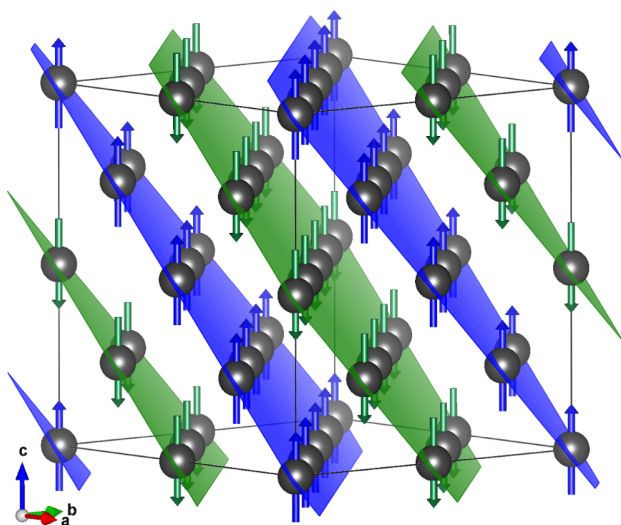


Figure S1: AFM-II magnetic structure represented in a  $2 \times 2 \times 2$  rock salt super cell. Alternate blue and green (111) lattice planes present the spin-up and spin-down planes, respectively.

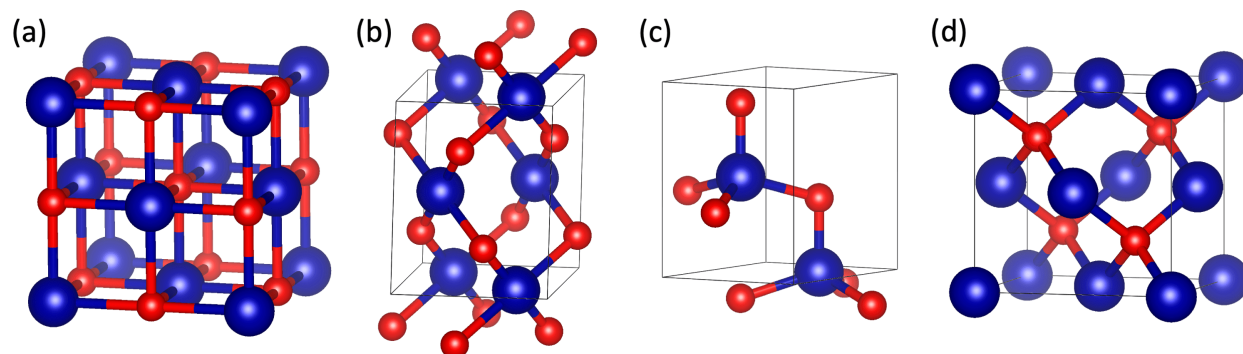


Figure S2: Structural models for (a) rock salt, (b) tenorite, (c) wurtzite, and (d) zinc belnde. Red spheres represent oxygen and blue atoms represent one of the  $A$ -site cations considered in this study,  $A = \{\text{Ca}, \text{Co}, \text{Cu}, \text{Fe}, \text{Mg}, \text{Mn}, \text{Ni}, \text{Zn}\}$

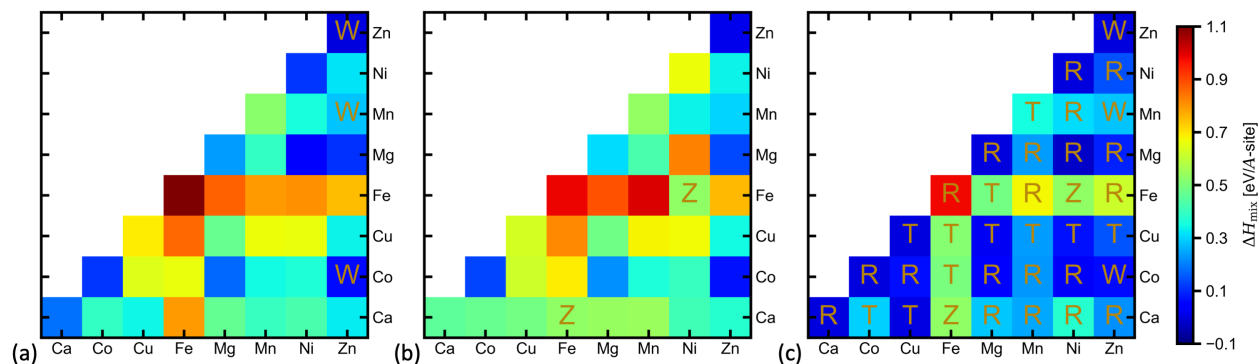


Figure S3: Heat maps for mixing enthalpy in eV/ $A$ -site of  $(AA')O$  ternary oxides in phase  $P$ ,  $E_M((AA')O, P)$ . The mixing enthalpies are shown for (a) wurtzite, (b) zinc belnde, and (c) ground phases. (c) Also shows the annotated ground phase for each  $A - A'$  combination. Only the lower triangular portion of the symmetric data is shown in all panels to avoid confusion. The color legend represents the mixing enthalpy in [eV/ $A$ -site] — blue and red represents low ( $\sim -0.1$ ) and high ( $\sim 1.1$ ) bond energies, respectively.

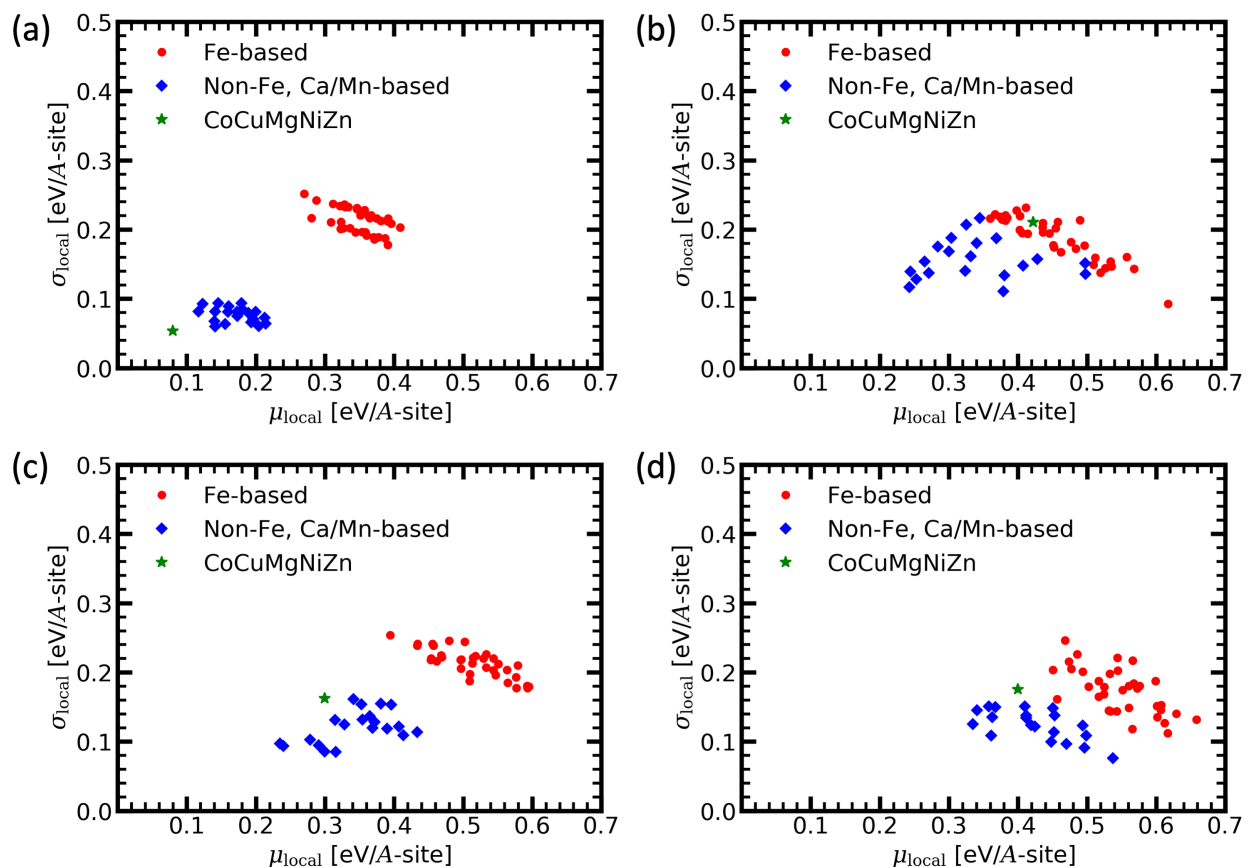


Figure S4: Comparison of enthalpy and entropy indicators,  $\mu_{\text{local}}$  and  $\sigma_{\text{local}}$ , respectively, for all 56 FCOs in (a) rock salt, (b) tenorite, (c) wurtzite, and (d) zinc blende structures. (1) Fe-based FCO cluster is shown in red, (2) Ca- or Mn-based (without Fe) FCO cluster is shown in blue, and (3) The entropy stabilized oxide — (CoCuMgNiZn)O — shown in green, is unique FCO with least- $\mu_{\text{local}}$  and least- $\sigma_{\text{local}}$  in rock salt structure.

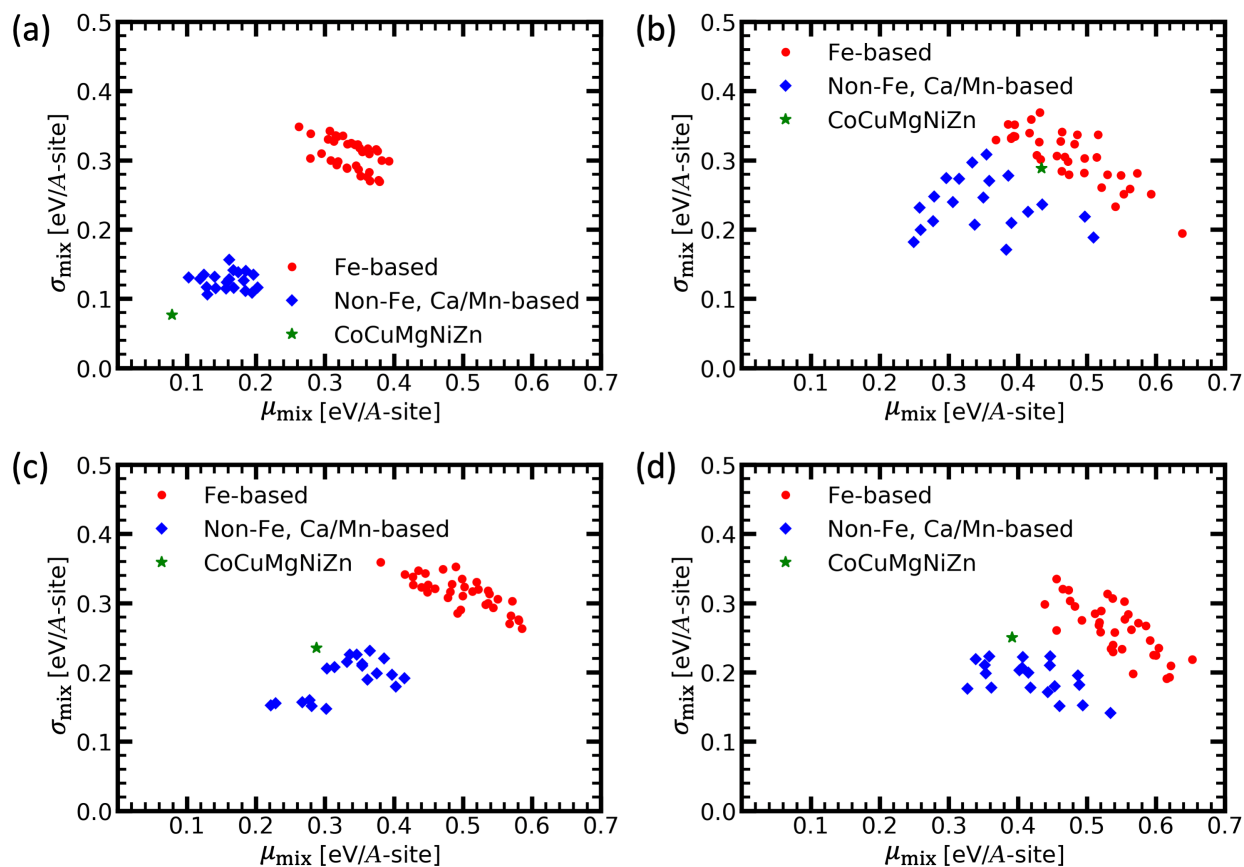


Figure S5: Comparison of enthalpy and entropy indicators,  $\mu_{\text{M}}$  and  $\sigma_{\text{M}}$ , respectively, for all 56 FCOs in (a) rock salt, (b) tenorite, (c) wurtzite, and (d) zinc blende structures. (1) Fe-based FCO cluster is shown in red circles, (2) Ca- or Mn-based (without Fe) FCO cluster is shown in blue diamonds, and (3) The entropy stabilized oxide — (CoCuMgNiZn)O — shown in green star, is unique FCO with least- $\mu_{\text{local}}$  and least- $\sigma_{\text{local}}$  in rock salt structure.

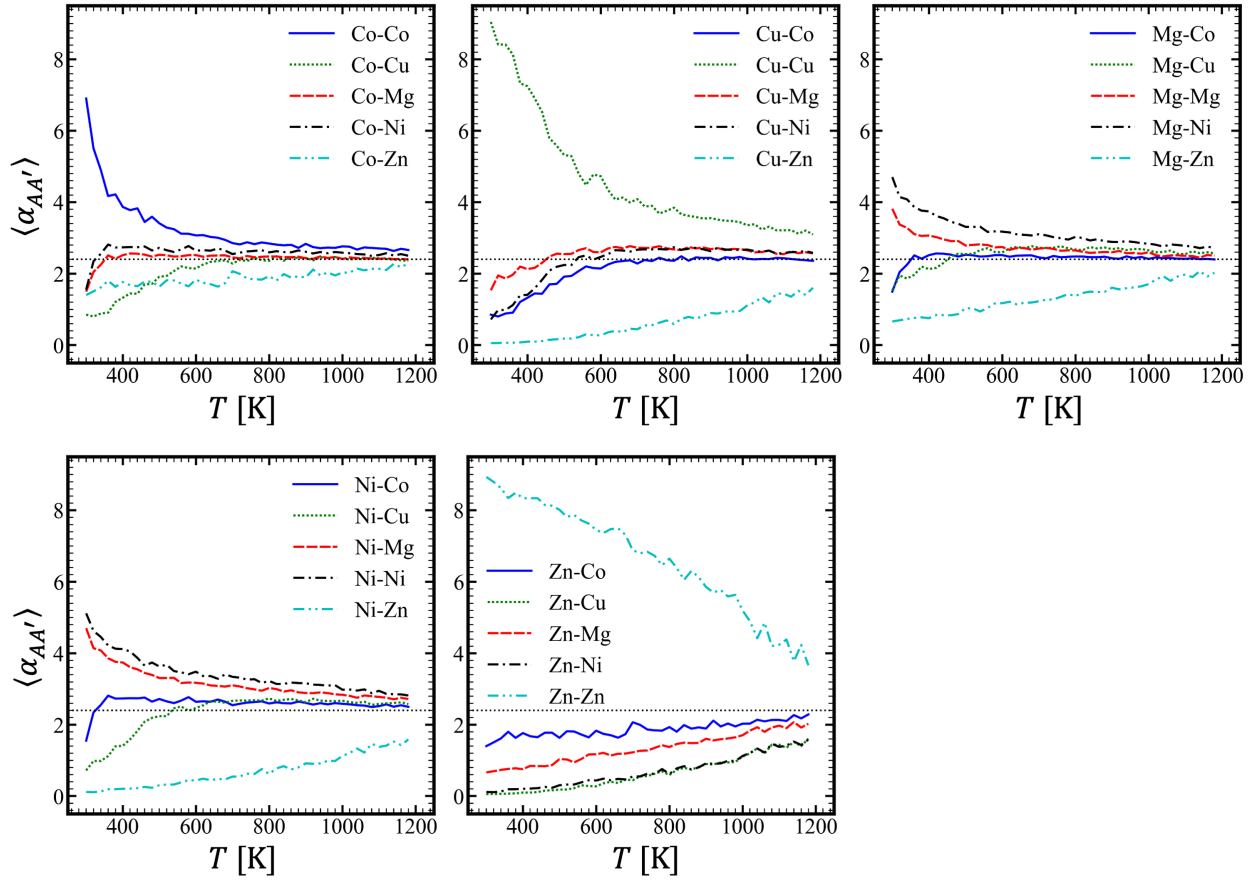


Figure S6: Short range order parameter plotted for all  $AA'$  combinations, as a function of temperature for the  $(\text{CoCuMgNiZn})\text{O}$ .

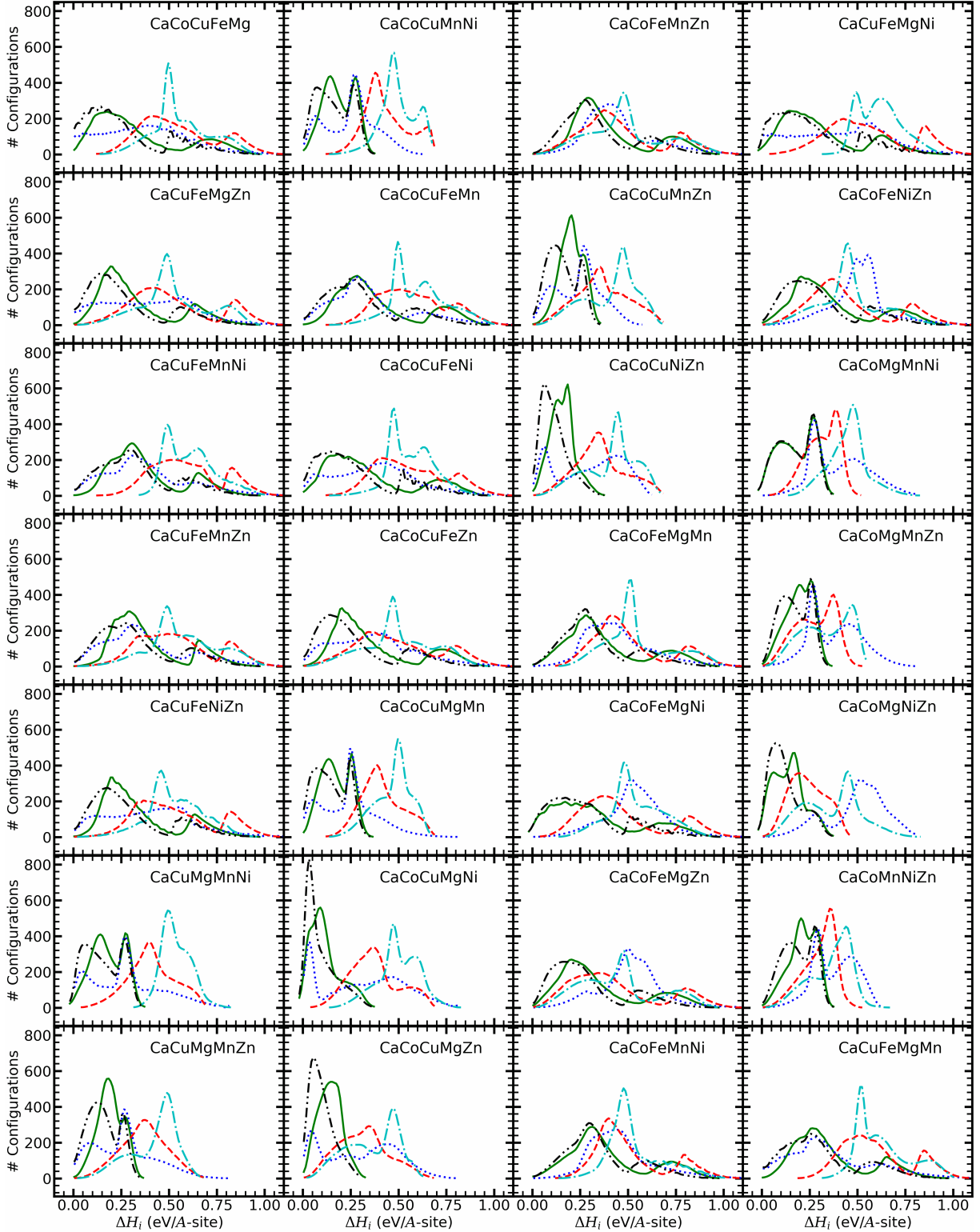


Figure S7: The distribution of the local mixing enthalpies of all possible local configurations for five component oxides (1 to 28), plotted in separate panel. Solid green, dotted blue, dashed red, dot-dashed cyan and black dot-dot-dashed lines represent distributions for rock salt, tenorite, wurtzite, zinc blende and ground phases, respectively.

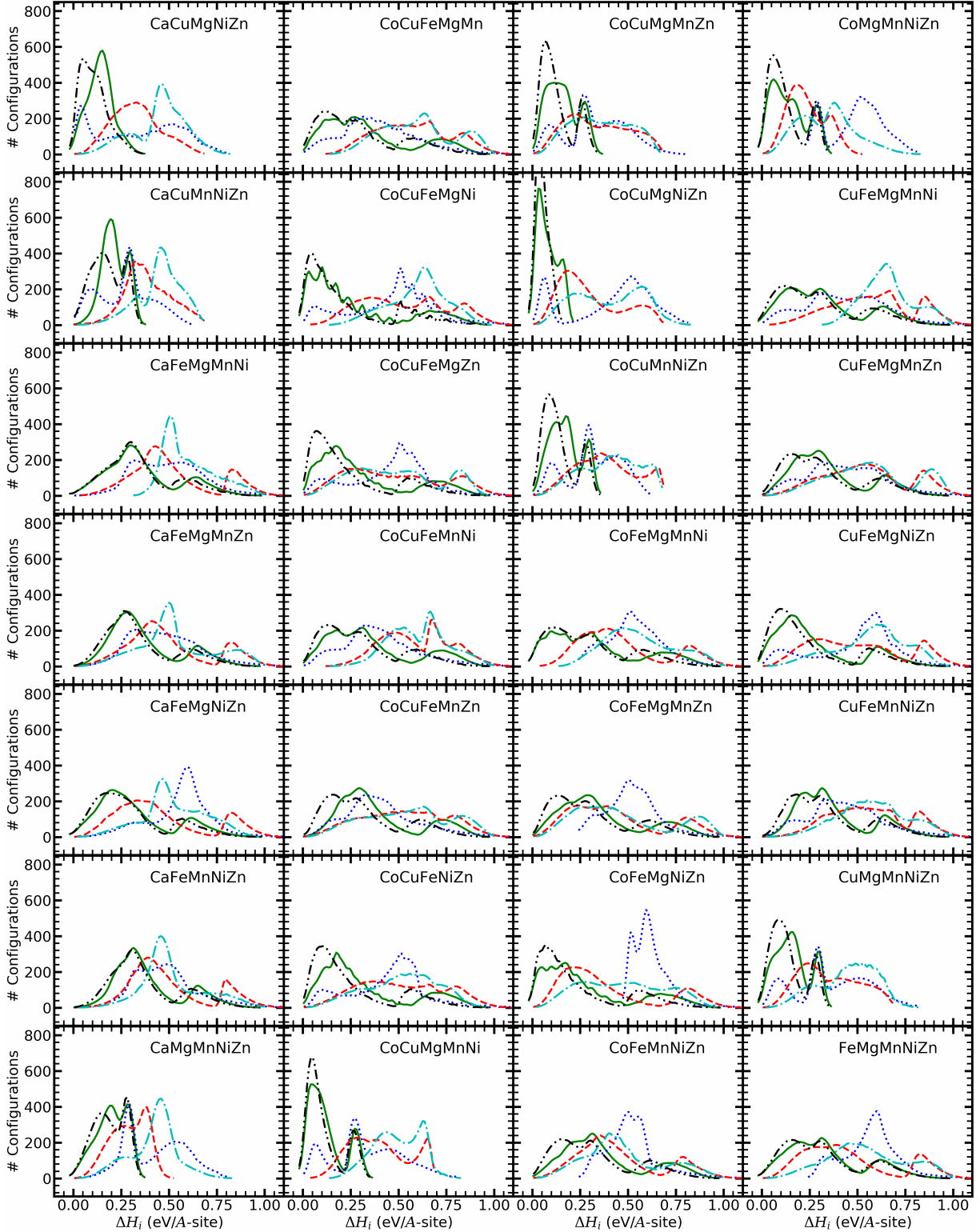


Figure S8: The distribution of the local mixing enthalpies of all possible local configurations for five component oxides (29 to 56), plotted in separate panel. Solid green, dotted blue, dashed red, dot-dashed cyan and black dot-dot-dashed lines represent distributions for rock salt, tenorite, wurtzite, zinc blende and ground phases, respectively.